Comparative ultrastructural characterisation of African horse sickness virus infected mammalian and insect cells reveals novel potential virus release mechanism from insect cells.

Running title: Ultrastructural characterisation of AHSV morphogenesis

Contents Category: Animal viruses – Double-strand RNA

Authors: E. Venter[1], C. F. van der Merwe[2], A.V. Buys[2], H. Huismans[1] and V. van Staden[1]

Author addresses:
1. Department of Genetics, University of Pretoria, Pretoria, 0002, South Africa.
2. Laboratory for Microscopy and Microanalysis, University of Pretoria, South Africa.

Correspondence to be sent to:

Vida van Staden
Department of Genetics
University of Pretoria
Private Bag X20
Hatfield
0028
South Africa
E-mail: vida.vanstaden@up.ac.za
+27 12 420 3257

Word count; summary: 245
Word count; main text: 5257
Number of figures: 4

SUMMARY

African horse sickness virus (AHSV) is an arbovirus capable of successfully replicating in both its mammalian host and insect vector. Where mammalian cells show a severe cytopathic effect (CPE) following AHSV infection, insect cells display no CPE. These differences in cell death could be linked to the method of viral release, i.e. lytic or non-lytic, that predominates in a specific cell type. Active release of AHSV, or any related orbivirus, has however not yet been documented from insect cells. We applied an integrated microscopy approach to compare the nanomechanical and morphological response of mammalian and insect cells to AHSV infection. Atomic force microscopy (AFM) revealed plasma membrane destabilisation, integrity loss and structural deformation of the entire surface of infected mammalian cells. Infected insect cells, in contrast, showed no morphological differences to mock-infected cells other than an increased incidence of circular cavities present on the cell surface. Transmission electron microscopy (TEM) imaging identified a novel large vesicle-like compartment within infected insect cells, not present in mammalian cells, containing viral proteins and virus particles. Extracellular clusters of aggregated virus particles were visualised adjacent to infected insect cells with intact plasma membranes. We propose that foreign material is accumulated within these vesicles and their subsequent fusion with the cell membrane will release entrapped viruses, thereby facilitating a non-lytic virus release mechanism different from the budding previously observed in mammalian cells. This insect cell-specific defence mechanism contributes to the lack of cell damage observed in AHSV infected insect cells.

INTRODUCTION

A common feature of arthropod borne viruses (arboviruses) is their ability to successfully infect different species, evident by the production of infectious progeny viruses from both mammalian hosts and insect vectors. Distinct differences are however observed in the effect of the viral infection on these species; with hosts exhibiting a range of clinical signs, whereas vectors remain unaffected (Mellor *et al.*, 2000; Mellor *et al.*, 2009). African horse sickness virus (AHSV) is an arbovirus and member of the family *Reoviridae* and genus *Orbivirus*, of which the closely related bluetongue virus (BTV) is the orbivirus prototype. AHSV is the etiological agent of African horse sickness (AHS), a World Organisation for Animal Health (OIE) listed notifiable disease of equids, with infection resulting in an equine mortality rate of up to 95% (Coetzer & Guthrie, 2004). Both AHSV and BTV are transmitted by *Culicoides* midge species. The occurrence of AHS and bluetongue is dependent on the distribution of the insect vectors, and recently changes in climatological factors such as global warming has resulted in the spread of these diseases to previously non-endemic areas (Gould & Higgs, 2009).

Orbiviruses are non-enveloped icosahedral viruses composed of a segmented double-stranded (ds) RNA genome enclosed by a dual-layered protein capsid (Mellor & Hamblin, 2004; Mertens & Diprose, 2004). The ten dsRNA genome segments encode seven structural (VP1-VP7) and four non-structural (NS1-NS4) proteins (Ratinier *et al.*, 2011; Roy *et al.*, 1994). The ±70 nm spherical virion consists of VP2 and VP5 forming the outer layer, and VP3 and VP7 that form the ±50 nm core particle composed of minor core proteins VP1, VP4, VP6 and ten dsRNA genome segments. Following virus adsorption and endocytosis, the outer coat proteins are removed and the core particle released into the cytoplasm. Transcription, translation and progeny virus assembly occur within the cytoplasm of infected cells. The most prominent manifestations of AHSV infection are the formation of large granular viral inclusion bodies (VIBs), and the assembly of thin tubular structures in the cytoplasm (Huismans & Els, 1979; Uitenweerde *et al.*, 1995). The matrix of the VIBs is composed of non-structural protein NS2, and these viral factories function as a scaffold for viral replication and assembly. The function of the tubules remains largely unknown, but they are comprised exclusively of multimers of the non-structural protein NS1. Following assembly at the periphery of the VIB, mature progeny viruses are transported to the plasma membrane for release by either a lytic or budding mechanism. The two non-structural proteins NS3 and NS3A, encoded from in-frame overlapping reading frames of genome segment 10, are involved in virus release (Stoltz *et al.*, 1996).

In AHSV infected cell culture, mammalian cells exhibit varying types of morphological changes culminating in death (Meiring *et al.*, 2009), whereas insect cells do not show any observable cytopathic effect (CPE) (Stassen *et al.*, 2012). It is postulated that in infected mammalian cells more lytic release occurs, whereas in insect cells only a non-lytic form of release such as budding takes place. Lytic release is characterised by cell membrane damage and disruption in the area of virus release, while budding in these non-enveloped viruses represents the process whereby a virus protrudes from the cell membrane and temporarily acquires a membrane envelope while leaving the plasma membrane intact (Beaton *et al.*, 2002; Han & Harty, 2004; Owens *et al.*, 2004).

One strategy of investigating this hypothesis is by means of ultrastructural characterisation of infected cells. To date the electron microscopy of AHSV has been focused on descriptions of life cycle events in mammalian cells and tissues (Breese *et al.*, 1969; Carrasco *et al.*, 1999; Gomez-Villamandos *et al.*, 1999), with no characterisation of AHSV infected insect cells. Thus it remains unclear whether the type of release mechanisms employed, other aspects of the AHSV life cycle, or the host cell response, could contribute to the absence of CPE and cell death in insect cells. This study represents the first ultrastructural comparison of AHSV morphogenesis in mammalian and insect cells. We applied an integrated microscopy approach to study both these cell types. Based on our results we propose an insect cell-specific defence mechanism that facilitates non-lytic virus release, different from the budding previously observed in mammalian cells, that contributes to the lack of cell damage in AHSV infected insect cells.

RESULTS

Cell morphology and mechanical properties of mock-infected and AHSV infected Vero and KC cells

Upon AHSV infection mammalian cells usually show severe CPE within the first 24 to 48 hours, whereas *Culicoides*-derived KC cells remain viable for more than two weeks. Atomic force microscopy (AFM) was used to investigate cell surface morphology and to quantify changes in nanomechanical properties of the plasma membranes of infected cells. Cells were fixed on coverslips in an attempt to immobilize any rare virus induced events at the cell membrane, and to prevent dislodging of non-fixed cells by the AFM tip. It has previously been established that the fixation conditions employed here would not significantly impact the structure or dimensions of the cells (Butt *et al.*, 1990).

AFM imaging was done on 50 mock-infected control cells and 50 AHSV infected mammalian Vero cells (Fig. 1a). Gross cell morphology was imaged from the peak force error channel (left panel) and three-dimensional height sensor measurements (middle panel), which were obtained by scanning an oscillating probe tip over the sample surface to record force-distance curves and sample height variations respectively. Mock-infected Vero cells (top panel) were elongated, 40 to 65 µm in size, and displayed a smooth membrane topography. Infected cells (bottom panel) were rounder, and exhibited an irregular topography with multiple protrusions on the cell surface. These protrusions ranged from 500 nm to 5 µm in diameter. The degree of membrane destabilisation, and areas displaying loss of integrity, was assayed using the deformation channel image (right panel). The deformation values were determined by exertion of a small but constant force on the cell surface by the microscope probe tip, and recording of the distance that the tip can deform the membrane at each point. Mock-infected cells displayed an average of 27.4 (±15.6) nm of deformation, with an approximately equal magnitude at any point of the cell surface. However in AHSV infected cells the average deformation increased by 50% to 41.5 (±23.5) nm. Areas of the surface that displayed the highest deformation values (yellow colouring) corresponded to the membrane protrusions visualised from the height sensor images. These membrane protrusion displayed deformation values ±2.5 times higher than the rest of the cell membranes, with values of up to 90 nm.

Cell morphology and membrane deformation changes can result from virus induced modifications of the cellular cytoskeleton network (Cai *et al.*, 2010). To investigate the effect of AHSV on the cytoskeleton, Vero cells were fixed, labelled with anti-tubulin markers and analysed by confocal laser scanning microscopy (Fig. 1b). These images confirmed the elongated shape of mock-infected versus rounding of virus infected cells described from the AFM profiles, and a slight redistribution of the microtubule network towards the cell periphery following AHSV infection, however overall the cells exhibited similar tubulin fibre distribution patterns. There was no sign of the total destruction of the normal microtubule network. Therefore AHSV infection does not induce major alterations to the cytoskeleton, but impacts on membrane integrity and cellular morphological and mechanical properties by another mechanism.

To investigate insect cells' response to AHSV infection, 50 mock-infected and 50 infected KC cells were analysed by AFM (Fig. 1c). Mock-infected cells (top panel) had a diameter of 7 to 20 µm, were round to slightly elongated in shape with a smooth membrane topography lacking any surface protrusions, and displayed an average deformation of 76.9 (±21.1) nm. One to three circular

indentations or cavities, ranging in diameter from 500 nm to 2.5 µm, were present on the cell surface of 20% of mock-infected cells. Virus infected cells (bottom panel) were similar to the control cells both in terms of morphology, and with respect to their membrane deformation values of 80.2 (±18.9) nm. The only difference was that in the infected sample there was a doubling of the number of cells that contained these cavities in their plasma membranes, with 42% of the cell population displaying cavities. The dimensions of the circular cavities from mock-infected and infected cells were within the same size range. Scanning electron microscopy (SEM) images of KC cells (Fig. 1d) confirmed the presence and size of these cavities identified by AFM.

Comparative ultrastructural characterisation of the virus life cycle in AHSV infected mammalian and insect cells

To examine the ultrastructural pathology of AHSV infection, two insect cell lines (KC and mosquito-derived C6/36 cells) and mammalian Vero cells were infected with AHSV, cryofixed and visualised by TEM. Infected insect cells were similar in cell size, shape, cytoplasmic density and organelle distribution to mock-infected cells, yet in addition displayed all the hallmarks of AHSV infection previously described in mammalian cells (Fig. 2). In a single section plane, up to three amorphous virus inclusion bodies (VIBs) of varying sizes could be detected in the cytoplasm of the majority of infected cells (Fig. 2a); immunogold labelling confirmed that they were composed of non-structural protein NS2 (Fig. 2a insert). Within the VIB protein matrix, dense circular virus core particles of ±50 nm could be observed. Mature ±70 nm spherical virions, which result from the assembly of the two outer capsid proteins onto the core, were usually present at the VIB periphery. Multiple virus particles were often arranged in a precise manner into a paracrystalline array (PCA) (Fig. 2b). Even though the PCAs could be present directly adjacent or in close proximity to VIBs, immunogold labelling indicated that they contained no NS2 protein (results not shown). Virus specific tubules (Fig. 2c) were abundant within the cytoplasm as well as in the nuclei. These ±23 nm wide, hollow tubules reached a length of up to 3 µm and were composed of non-structural protein NS1 (Fig. 2c insert). Rectangular crystalline structures of varying size were observed within the cytoplasm (Fig. 2d), or rarely within nuclei. These structures were similar to the "cytoplasmic inclusions" or "lamellar structures" first described by Breese in 1969 (Breese & Ozawa, 1969; Breese *et al.*, 1969). Up to three of these crystalline particles, ranging from 75 to 650 nm in width and 800 nm to 5 µm in length, with no specific width to length ratio, were found in the majority of cells. Strong and specific labelling with an anti-VP7 antibody (Fig. 2d insert) confirmed that these structures represent the hexagonal VP7 crystals which can be purified from AHSV infected cells (Burroughs *et al.*, 1994).

Upon higher magnification, it was observed that these particles had a sheeted appearance (Fig. 2e), corresponding to the highly ordered two-dimensional crystalline lattice structure described for the purified VP7 crystals (Burroughs *et al.*, 1994). Occasionally, mature virions or NS1 tubules were observed in close association with the VP7 crystals, but this was not deemed to be of functional significance.

A novel structure was observed in insect cells not previously identified in AHSV infected mammalian cells. In both KC and C6/36 cells a number of large, circular, membrane bound vesicle-like structures ranging in size from 500 nm to 5 µm were present. In mock-infected control cells these vesicles could either be empty (Fig. 3a), or contained some cellular debris (Fig. 3b). However in infected cells, these structures usually contained viral material (Fig. 3c, d). We observed multiple mature virus particles and immature cores within these vesicles (Fig. 3c insert), as well as VP7 crystalline structures and NS1 tubules (Fig. 3e, f). The virus-specific nature of all of these was confirmed by immunogold labelling (not shown). Interestingly, labelling with anti-NS1 or anti-NS2 antibodies gave significantly stronger positive signals within the vesicles than in the cytoplasm, even when no tubules or VIBs could be discerned. This could indicate some preferential inclusion of cytoplasmic material containing foreign proteins into the vesicles. These vesicles were sometimes observed in very close proximity to the plasma membrane (Fig. 3g). Similar vesicle-like structures were documented in BTV infected *Culicoides* cells (Celma & Roy, 2011), however the authors only observed multiple fully packaged viruses but no other viral material inside the vesicles.

Orbivirus release from insect cells has long been postulated to be primarily non-lytic, as virus infection results in no observable cytopathic effect. In an attempt to observe this release, we meticulously screened more than 300 cells, but were never able to capture any budding-type event similar to that observed in mammalian cells (see below). We even cultured and processed the cells directly in 200 µm diameter cellulose microcapillary tubes, as we recently reported that this reduces mechanical disruption and increases the chance of observing virus release (Venter *et al.*, 2012), but with no success. We however visualised extracellular viruses, present either as individual particles or as clusters of aggregated viruses, between neighbouring infected cells with intact plasma membranes (Fig. 3h). These virus particles were not remnants of the viral inoculum, as samples processed one hour post infection did not exhibit any extracellular viruses (results not shown). From these data we propose that AHSV is rarely or never released directly from the insect cell cytoplasm by budding, but rather by fusion of the large virus-containing vesicles with the plasma membrane.

For comparison to the insect cells, we also viewed mammalian cells by TEM (Fig. 4). Earlier reports on the ultrastructure of AHSV infected mammalian tissue (Breese *et al.*, 1969; Carrasco *et al.*, 1999; Gomez-Villamandos *et al.*, 1999; Lecatsas & Erasmus, 1967) used conventional chemical fixation. However sample preparation by cryofixation through high-pressure freezing and freeze-substitution (HPF-FS) as used here yields increased sample quality and membrane preservation (Studer *et al.*, 2001), which can be crucial for TEM visualisation of plasma membrane virus release events (Hawes *et al.*, 2007). From the micrographs the gross morphological structure of infected Vero cells correlated with that observed by AFM. The cells did not retain their elongated shape, but became rounder and exhibited multiple membrane protrusions (Fig. 4a). The other typical virus-induced structures were also present, e.g. VIBs, PCAs, VP7 crystals and NS1 tubules (not shown). Based on our description of the vesicle-like structures containing virus material in insect cells, we carefully examined mammalian cells for the presence of similar components. In about 5% of cells there were small vesicles, ranging in size from 100 – 500 nm, which contained one to five virus particles (Fig. 4b, c). Occasionally the merging of such a vesicle with the membrane was observed (Fig. 4d). We postulated that at this late stage of the infection cycle (48 hpi) it represented the release of a mature virion, rather than an entry event. These vesicles did not contain any other cytoplasmic or viral material. However the bulk of virus release appeared to be through a lytic process, where extensive membrane damage occurred in close proximity to extracellular virus particles (Fig. 4e). In less than 2% of cells we recorded a non-lytic budding-type release, where an individual virus particle protruded through the membrane without any visible membrane damage (Fig. 4f).

DISCUSSION

The exact nature of the cellular response to AHSV infection, the differences in induction of a cell death response in different cell types, and the contribution of AHSV morphogenesis to these is not fully understood. This study represents an ultrastructural comparison of AHSV infected mammalian and insect cells using atomic force microscopy (AFM), scanning electron microscopy (SEM), transmission electron microscopy (TEM) and confocal fluorescence microscopy.

Initially AFM was used to examine cell morphology in response to viral infection. This is the first study using AFM for orbiviruses. The AFM profiles of AHSV infected Vero cells revealed a highly uneven plasma membrane topology and an increased deformability in comparison to mock-infected controls. The change in membrane integrity was not uniform across the cell surface. The areas where the largest cell surface protrusions or membrane blebs were identified from the three-

dimensional scans, also showed the biggest deformation ability when probed by the microscope tip. This indicates that the membrane changes are not a generalised response to e.g. the release of chemical inflammatory mediators (Carrasco *et al.*, 1999). We also ruled out the possibility that the surface disruption was the result of underlying modifications to the cytoskeletal structure upon virus infection, as is induced by e.g. rotavirus replication in cell culture (Yang & McCrae, 2012), as the microtubule network organisation in AHSV infected cells only showed minor redistribution.

These surface protrusions could be membrane blebs formed as a result of the infected cells undergoing apoptosis (Stassen *et al.*, 2012), similar to what was observed by SEM for BTV (Nagaleekar *et al.*, 2007). Alternatively, these bulges could be areas where localised membrane destabilisation has occurred prior to virus egress by lytic release. Immunofluorescence microscopy showed that in BTV infected cells the viral outer capsid protein VP5, together with non-structural protein NS3, co-localise in small patches at the plasma membrane (Bhattacharya & Roy, 2008). NS3 is capable of binding to both cellular membrane trafficking proteins and to the viral capsid to mediate virus release (Beaton *et al.*, 2002; Wirblich *et al.*, 2006), and AHSV NS3 is present in membrane fragments close to areas of lytic virus release (Stoltz *et al.*, 1996). What remains unclear in AHSV infected cells is the link between the virus-induced membrane permeability changes, and the membrane deformation observed here. We previously showed that NS3 can act as a viroporin in the AHSV life cycle by altering membrane permeability and facilitating virus release, however the degree of membrane permeabilization induced by different AHSV strains did not correspond to the level of CPE observed (Meiring *et al.*, 2009). The localisation of AHSV NS3 and / or capsid proteins to the regions of membrane protrusion could be investigated by AFM combined with antibody tip modifications.

TEM of Vero cells confirmed the major disruption of cell morphology and plasma membrane integrity following AHSV infection. Cells exhibited characteristics both of apoptosis such as chromatin condensation, membrane blebbing and apoptotic bodies, and of necrosis such as cell rounding and swelling, and loss of membrane integrity (Galluzzi *et al.*, 2012). We verified that virus release from a mammalian cell line is mostly via a lytic process, and also occasionally from a budding-type event. We also for the first time described the presence of small cytoplasmic vesicles containing one or a few virions. Similar structures have been observed in BTV infected cells, and were proposed to be either endosomal entry events at early times post infection (Eaton *et al.*, 1990) or budding of virions into cytoplasmic vesicles that occurred late in the course of infection (Brewer & MacLachlan, 1994). Both BTV and AHSV NS3 can interact with Tsg101 (Wirblich *et al.*, 2006), a

member of the ESCRT protein complex involved in governing the biogenesis/degradation of multivesicular bodies (MVBs) (Babst, 2005). MVBs can either traffic to lysosomes where they are subjected to proteosomal degradation (termed 'degradative MVBs'), or alternatively to the plasma membrane where they fuse with the membrane and release their contents into the extracellular space (the 'exocytic MVBs') (Mathivanan *et al.*, 2010). Based on the late times after infection that they were present, and the presence of multiple viruses in these vesicles, we postulate that the observed vesicles function as exocytic MVBs that allow temporary storage for completely packaged viruses, and serve as an additional mechanism to facilitate virus release.

The AFM and SEM profiles of the AHSV infected KC cells showed unchanged morphology and mechanical properties when compared to uninfected cells. This correlated with the previously documented lack of insect cell damage following BTV and AHSV infection (Stassen *et al.*, 2012; Wechsler & McHolland, 1988). However we observed a 100% increase in the prevalence of large circular cavities present on the cell surface following virus infection. TEM imaging of cell sections identified membrane-bound vesicular compartments in the cytoplasm of both uninfected and AHSV infected insect cells, corresponding in size to the cavities. We therefore propose that the cavities imaged by AFM represent the merging of these cytoplasmic vesicles with the plasma membrane, thereby enabling the release of their content, and that AHSV infection either increases the number of these vesicles, or the rate at which they fuse with cell membrane.

In contrast to the normally empty status of the vesicles in mock-infected cells, those in AHSV infected cells usually contained viral proteins or virus particles. This might thus represent a cellular defence mechanism, activated by viral infection, whereby any foreign material could be stored within these vesicle-like structures for subsequent expulsion. It is unlikely that AHSV replication occurred within the vesicles, as VIBs were never observed within them. It is not known whether these vesicles are autophagosomes. Autophagy is a cellular process that targets cytoplasmic components for autodigestion, but is also important in innate and adaptive immunity and controlling intracellular microbes (Deretic & Levine, 2009). A number of viruses have been shown to subvert the autophagy response by either promoting virus replication or by enabling non-lytic viral release (Lin *et al.*, 2010). Autophagy was also proven to play a direct antiviral role against the mammalian pathogen vesicular stomatitis virus (VSV) in the insect Drosophila (Shelly *et al.*, 2009). Autophagosomes are normally distinguished by the presence of a double-layered membrane, the source of these membranes is suggested to be primarily from the ER (Juhasz & Neufeld, 2006). Although some of the vesicles we observed contained a double membrane (not shown), the majority

of these structures were enclosed by a single-layered membrane. Due to the fast turnover of the fusion of autophagosomes with lysosomes which results in inner membrane loss, and the prolonged infection times utilised here, these single-membrane structures could well represent autolysosomes (Deretic & Levine, 2009).

The difficulty in visualising active virus release events from infected insect cells confirmed our lack of understanding of virus transport in and release from these cells. The sequestration of a large fraction of the infectious AHSV particles into a vesicular compartment in insect vector cells could also account for the absence of CPE in cell culture and the lack of any deleterious effect of viral infection on the *Culicoides* vector. Our observation of aggregated virus particles outside infected insect cells, which showed no membrane damage, supported the view that viruses were being released en masse via a non-lytic release mechanism.

Similar virus-containing vesicles were described in BTV infected insect cells, however there the simultaneous expression of both NS3 and NS3A were required for vesicle formation (Celma & Roy, 2011). Mutant BTV viruses lacking either NS3 or NS3A showed attenuation of viral replication, absence of vesicles, virus particles scattered throughout the cytosol, and reduction of virus release. As no budding from the plasma membrane was ever observed from BTV infected KC cells (Celma & Roy, 2011), the mechanism of release of these mutant viruses from insect cells remains unclear. Peruvian horse sickness virus, another member of the *Orbivirus* genus, was associated with vesicles in C6/36 cells (Attoui *et al.*, 2009), but these were small vesicle containing only one or two virus particles. Rice dwarf virus (RDV), also a member of the *Reoviridae* family that is able to replicate in plants and insects, utilises vesicles in insect vector cells morphologically very similar to those we have described here (Wei *et al.*, 2008). It was proposed that RDV particles are assembled at the periphery of the viroplasm (the equivalent of the AHSV VIBs), engulfed by the vesicular compartments, and subsequently released upon fusion of these compartments with the cell membranes.

The outcome of this study was the first ultrastructural comparison between AHSV infected insect and mammalian cells. We hypothesise that the lack of cell death observed in infected insect cells is at least partly due to a distinct cellular response resulting in the accumulation of viral material into vesicle-like structures. These vesicles then merge with the plasma membrane to release all of the contents, including virus particles, thereby facilitating a non-lytic form of release. This insight into

the insect cell response to AHSV infection should be expanded by analyses focusing on AHSV NS3 distribution and function, vesicular trafficking and host autophagy response pathways.

METHODS

Cells and viruses

Vero cells (ATCC CCL-81) were cultured in the presence of Eagle's Minimal Essential Medium (MEM) supplemented with 5% fetal calf serum (FCS), antibiotics and antifungals (penicillin, streptomycin and fungizone) at 37°C in 5% CO_2. KC cells (derived from *Culicoides variipennis)* obtained from Onderstepoort Veterinary Institute (OVI), South Africa, were cultured at 28°C in modified Schneider's *Drosophila* medium supplemented with 10% FCS, antibiotics and antifungals. C6/36 cells (*Aedes albopictus*) (ATCC CRL-1660) were cultured at 28°C in MEM supplemented with 10% FCS, 1% pyruvate, antibiotics and antifungals.

AHSV serotype 3 (AHSV-3) was obtained from the OIE Reference Laboratory at OVI, South Africa. AHSV-3 stocks were generated by infecting Vero cells at a low multiplicity of infection (MOI), harvesting the cells when sufficient CPE was exhibited, and stored at 4°C. Virus titres were determined by plaque assay as previously described (Meiring *et al.*, 2009).

Cells were cultured either upon glass coverslips until ±75% confluent for AFM, SEM and confocal imaging, or cultured as a monolayer on culture flasks for TEM visualisations as previously described (Venter *et al.*, 2012). KC and C6/36 cells were infected with AHSV-3 at a MOI of 0.5 plaque forming units per cell and Vero cells at a MOI of 5. The virus inoculum was removed after one hour of adsorption and replaced with fresh medium. Vero cells were processed 24 to 48 hours post infection (hpi), and KC and C6/36 cells seven days post infection (dpi).

AFM analysis

Coverslips with infected cells were washed twice with phosphate buffered saline (PBS) solution and fixed with 2.5% glutaraldehyde/formaldehyde in PBS for 30 minutes. The samples were imaged with a Bruker (Dimension Icon with ScanAsyst) atomic force microscope in the Peak Force Quantitative Nanomechanical Mapping (QNM) imaging mode. A triangular silicon nitride cantilever with a 20 nm radius tip was used to scan at a speed of 0.2 to 0.5 Hz with resonant frequency of probe tip oscillations at 150 kHz.

SEM analysis

Coverslips with infected KC cells were washed twice with PBS. Cells were then fixed with 0.5% aqueous osmium tetroxide, followed by ethanol dehydration, hexamethyldisilazane (HMDS) treatment and carbon coating. Images were acquired with a Zeiss Ultra Plus FEG-SEM, operated at 1kV and a working distance of 2 mm.

Confocal laser scanning microscopy

Coverslips with infected Vero cells were washed with PBS, fixed with 4% paraformaldehyde for 30 minutes, and incubated in blocking solution (5% milk powder in PBS) for 30 minutes. Primary labelling was done with anti-β-tubulin (Sigma) antibody diluted 1:100 in blocking solution overnight at 4°C, followed by three consecutive five minute washes with 0.5% Tween in PBS. Secondary labelling was with anti-mouse Alexa Fluor® 594 (Invitrogen) diluted 1:250 in blocking solution for one hour at room temperature (RT). After another set of washes, the coverslips were mounted onto microscope slides using VECTASHIELD mounting medium (Vector Laboratories) and analysed with a Zeiss LSM 510 Meta Confocal Laser Scanning Microscope.

High-pressure freezing and freeze-substitution

Infected cells cultured as a monolayer were dislodged by scraping, concentrated by low speed centrifugation and the cell pellet transferred to a Leica membrane sample carrier. High-pressure freezing (HPF) was done with the LEICA EMPACT2 HPF apparatus followed by freeze substitution (FS) in a LEICA AFS2 FS machine.

Resin embedding, ultrathin sectioning

Resin embedding was done in Quetol 651 epoxy resin (Van der Merwe & Coetzee, 1992) or LR White resin (SPI Supplies) for ultrastructural analyses and immunogold labelling respectively. Ultrathin sections (100 nm) were made with a Reichert-Jung Ultracut E microtome with a Diatome diamond knife.

Immunogold labelling

Immunogold labelling was done with a variety of AHSV specific antibodies. Antibodies directed against NS2 or VP7 respectively were raised in rabbits (Uitenweerde *et al.*, 1995) or guinea-pigs (Rutkowska *et al.*, 2011) against these proteins expressed in insect cells by the baculovirus system. The rabbit anti-NS1 serum (GenScript) was directed against a synthetic peptide representing amino acids 489-503 of NS1. Ultrathin cell sections on carbon grids were blocked in potassium phosphate

buffer (PPB) containing 5% FCS and 0.05% Tween for 30 min. Grids were transferred to a drop of primary antibody diluted 1:100 in blocking solution, incubated for two hours at RT, and washed twice consecutively for two minutes each in blocking solution, PPB and dH_2O. Secondary labelling was done for one hour with either anti-rabbit or anti-guinea-pig 10 nm colloidal gold conjugate (SPI Supplies) diluted 1:20 in blocking solution and samples washed as above.

Staining and TEM viewing

Ultrathin sections from Quetol embedded and immunogold labelled LR White samples were stained for 15 minutes in 1% uranyl acetate and three minutes in Reynolds' lead citrate (Reynolds, 1963). TEM visualization was done with a JEOL JEM-2100F field emission transmission electron microscope.

Figure Legends

Fig. 1. Morphological and nanomechanical cell response of Vero and KC cells to AHSV infection. (a) Atomic force microscope (AFM) imaging of Vero cells that were mock (top panel) or AHSV infected (bottom panel) at 24hpi. All images were acquired in QNM mode, and represent the peak force error (left column), height sensor (middle column) and deformation channels (right column). Membrane protrusions in infected cells are indicated by arrows. (b) Immunofluorescence of mock (top) or AHSV infected (bottom) Vero cells stained with anti-β-tubulin antibody followed by Alexa-594-conjugated anti-mouse antibody. (c) AFM images of mock (top panel) or AHSV infected (bottom panel) *Culicoides*-derived KC cells at 7 dpi, imaged as in (a). (d) SEM imaging of mock (top panel) or AHSV infected (bottom panel) KC cells. Circular indentations in the membrane are indicated by squares. Colour scale of deformation channel images range from 0 (black) to 200 (white) nm for Vero cells, and 0 – 220 nm for KC cells. Bars, 10 µm (a – c); 1 µm (d).

Fig. 2. Ultrastructure of AHSV infected KC cells illustrating structures associated with viral replication. (a - e) KC cells were infected with AHSV at a MOI of 0.5, processed 7 dpi and fixed by HPF-FS. Virus inclusion body (VIB), paracrystalline array (PCA), tubules (Tub) and crystalline structures (Cr) are indicated. (Inserts) Immunogold labelling with (a) anti-NS2, (c) anti-NS1 and (d) anti-VP7 antibodies respectively illustrates the protein component of the VIBs, tubules and crystalline structures. Bars, 2 µm (a); 500 nm (b – e and inserts).

Fig. 3. Ultrastructure of C6/36 and KC cells illustrating intracellular vesicles and virus release. (a, b) Mock-infected C6/36 cells harbour empty vesicles (arrows) or occasionally vesicles containing some cellular material (arrowheads). (c - h) Cells were infected with AHSV at a MOI of 0.5, processed 7 dpi and fixed by HPF-FS. (c) Large vesicle-like structures in C6/36 cells containing core and virus particles. Insert: core particles (C) and virions (V) can be distinguished based on size and presence of the outer capsid. (d) Large vesicle-like structure containing virus material. (e, f) Enlargement of the demarcated areas from b, indicating crystalline structures (Cr) and tubules (Tub). (g) Vesicle adjacent to plasma membrane. (h) Extracellular clusters of aggregated viruses (stars), and individual particles (V) between intact plasma membranes of infected KC cells. Bars, 2 µm (a – c, e); 200 nm (insert); 500 nm (d, f - h).

Fig. 4. Ultrastructure of AHSV infected Vero cells. Vero cells were infected with AHSV at a MOI of 5, processed 48 hpi and fixed by HPF-FS. (a) Cells have irregular plasma membranes containing

multiple membranous protrusions (arrowheads). (b, c) Small intracellular vesicles containing up to five virus particles (arrows). (d) A single virus-containing vesicle merging with the plasma membrane. (e) Virus particles (arrows) in close proximity to a damaged membrane (star). (f) Virus particles budding from the cell surface. Bars, 4 µm (a); 500 nm (b-f).

ACKNOWLEDGEMENTS

The authors thank Mr Flip Wege for valuable technical assistance. Financial assistance was provided by the National Research Foundation, Poliomyelitis Research Foundation and the Microscopy Society of Southern Africa Trust.

REFERENCES

Attoui, H., Mendez-Lopez, M. R., Rao, S., Hurtado-Alendes, A., Lizaraso-Caparo, F., Jaafar, F. M., Samuel, A. R., Belhouchet, M., Pritchard, L. I., Melville, L., Weir, R. P., Hyatt, A. D., Davis, S. S., Lunt, R., Calisher, C. H., Tesh, R. B., Fujita, R. & Mertens, P. P. (2009). Peruvian horse sickness virus and Yunnan orbivirus, isolated from vertebrates and mosquitoes in Peru and Australia. *Virology* **394**, 298-310.

Babst, M. (2005). A protein's final ESCRT. *Traffic* **6**, 2-9.

Beaton, A. R., Rodriguez, J., Reddy, Y. K. & Roy, P. (2002). The membrane trafficking protein calpactin forms a complex with bluetongue virus protein NS3 and mediates virus release. *Proc Natl Acad Sci U S A* **99**, 13154-13159.

Bhattacharya, B. & Roy, P. (2008). Bluetongue virus outer capsid protein VP5 interacts with membrane lipid rafts via a SNARE domain. *J Virol* **82**, 10600-10612.

Breese, S. S., Jr. & Ozawa, Y. (1969). Intracellular inclusions resulting from infection with African horsesickness virus. *J Virol* **4**, 109-112.

Breese, S. S., Jr., Ozawa, Y. & Dardiri, A. H. (1969). Electron microscopic characterization of African horse-sickness virus. *J Am Vet Med Assoc* **155**, 391-400.

Brewer, A. W. & MacLachlan, N. J. (1994). The pathogenesis of bluetongue virus infection of bovine blood cells in vitro: ultrastructural characterization. *Arch Virol* **136**, 287-298.

Burroughs, J. N., O'Hara, R. S., Smale, C. J., Hamblin, C., Walton, A., Armstrong, R. & Mertens, P. P. (1994). Purification and properties of virus particles, infectious subviral particles, cores and VP7 crystals of African horsesickness virus serotype 9. *J Gen Virol* **75 (Pt 8)**, 1849-1857.

Butt, H. J., Wolff, E. K., Gould, S. A., Dixon Northern, B., Peterson, C. M. & Hansma, P. K. (1990). Imaging cells with the atomic force microscope. *Journal of structural biology* **105**, 54-61.

Cai, X., Xing, X., Cai, J., Chen, Q., Wu, S. & Huang, F. (2010). Connection between biomechanics and cytoskeleton structure of lymphocyte and Jurkat cells: An AFM study. *Micron* **41**, 257-262.

Carrasco, L., Sanchez, C., Gomez-Villamandos, J. C., Laviada, M. D., Bautista, M. J., Martinez-Torrecuadrada, J., Sanchez-Vizcaino, J. M. & Sierra, M. A. (1999). The role of pulmonary intravascular macrophages in the pathogenesis of African horse sickness. *J Comp Pathol* **121**, 25-38.

Celma, C. C. & Roy, P. (2011). Interaction of calpactin light chain (S100A10/p11) and a viral NS protein is essential for intracellular trafficking of nonenveloped bluetongue virus. *J Virol* **85**, 4783-4791.

Coetzer, J. A. W. & Guthrie, A. J. (2004). *African Horse sickness. In Infectious Diseases of Livestock*. Cape Town: Oxford University Press Southern Africa.

Deretic, V. & Levine, B. (2009). Autophagy, immunity, and microbial adaptations. *Cell host & microbe* **5**, 527-549.

Eaton, B. T., Hyatt, A. D. & Brookes, S. M. (1990). The replication of bluetongue virus. *Curr Top Microbiol Immunol* **162**, 89-118.

Galluzzi, L., Vitale, I., Abrams, J. M., Alnemri, E. S., Baehrecke, E. H., Blagosklonny, M. V., Dawson, T. M., Dawson, V. L., El-Deiry, W. S., Fulda, S., Gottlieb, E., Green, D. R., Hengartner, M. O., Kepp, O., Knight, R. A., Kumar, S., Lipton, S. A., Lu, X., Madeo, F., Malorni, W., Mehlen, P., Nunez, G., Peter, M. E., Piacentini, M., Rubinsztein, D. C., Shi, Y., Simon, H. U., Vandenabeele, P., White, E., Yuan, J., Zhivotovsky, B., Melino, G. & Kroemer, G. (2012). Molecular definitions of cell death subroutines: recommendations of the Nomenclature Committee on Cell Death 2012. *Cell death and differentiation* **19**, 107-120.

Gomez-Villamandos, J. C., Sanchez, C., Carrasco, L., Laviada, M. M., Bautista, M. J., Martinez-Torrecuadrada, J., Sanchez-Vizcaino, J. M. & Sierra, M. A. (1999). Pathogenesis of African horse sickness: ultrastructural study of the capillaries in experimental infection. *J Comp Pathol* **121**, 101-116.

Gould, E. A. & Higgs, S. (2009). Impact of climate change and other factors on emerging arbovirus diseases. *Trans R Soc Trop Med Hyg* **103**, 109-121.

Han, Z. & Harty, R. N. (2004). The NS3 protein of bluetongue virus exhibits viroporin-like properties. *J Biol Chem* **279**, 43092-43097.

Hawes, P., Netherton, C. L., Mueller, M., Wileman, T. & Monaghan, P. (2007). Rapid freeze-substitution preserves membranes in high-pressure frozen tissue culture cells. *J Microsc* **226**, 182-189.

Huismans, H. & Els, H. J. (1979). Characterization of the tubules associated with the replication of three different orbiviruses. *Virology* **92**, 397-406.

Juhasz, G. & Neufeld, T. P. (2006). Autophagy: a forty-year search for a missing membrane source. *PLoS biology* **4**, e36.

Lecatsas, G. & Erasmus, B. J. (1967). Electron microscopic study of the formation of african horse-sickness virus. *Arch Gesamte Virusforsch* **22**, 442-450.

Lin, L.-T., Dawson, P. W. H. & Richardson, C. D. (2010). Viral interactions with macroautophagy: A double-edged sword. *Virology* **402**, 1-10.

Mathivanan, S., Ji, H. & Simpson, R. J. (2010). Exosomes: extracellular organelles important in intercellular communication. *Journal of proteomics* **73**, 1907-1920.

Meiring, T. L., Huismans, H. & van Staden, V. (2009). Genome segment reassortment identifies non-structural protein NS3 as a key protein in African horsesickness virus release and alteration of membrane permeability. *Arch Virol* **154**, 263-271.

Mellor, P. S., Boorman, J. & Baylis, M. (2000). Culicoides biting midges: their role as arbovirus vectors. *Annu Rev Entomol* **45**, 307-340.

Mellor, P. S., Carpenter, S. & White, D. M. (2009). BTV in the insect host: in Bluetongue virus, biology of animal infections. 295-320.

Mellor, P. S. & Hamblin, C. (2004). African horse sickness. *Veterinary research* **35**, 445-466.

Mertens, P. P. & Diprose, J. (2004). The bluetongue virus core: a nano-scale transcription machine. *Virus Res* **101**, 29-43.

Nagaleekar, V. K., Tiwari, A. K., Kataria, R. S., Bais, M. V., Ravindra, P. V. & Kumar, S. (2007). Bluetongue virus induces apoptosis in cultured mammalian cells by both caspase-dependent extrinsic and intrinsic apoptotic pathways. *Arch Virol* **152**, 1751-1756.

Owens, R. J., Limn, C. & Roy, P. (2004). Role of an arbovirus nonstructural protein in cellular pathogenesis and virus release. *J Virol* **78**, 6649-6656.

Ratinier, M., Caporale, M., Golder, M., Franzoni, G., Allan, K., Nunes, S. F., Armezzani, A., Bayoumy, A., Rixon, F., Shaw, A. & Palmarini, M. (2011). Identification and characterization of a novel non-structural protein of bluetongue virus. *PLoS pathogens* **7**, e1002477.

Reynolds, E. S. (1963). The use of lead citrate at high pH as an electron-opaque stain in electron microscopy. *J Cell Biol* **17**, 208-212.

Roy, P., Mertens, P. P. & Casal, I. (1994). African horse sickness virus structure. *Comp Immunol Microbiol Infect Dis* **17**, 243-273.

Rutkowska, D. A., Meyer, Q. C., Maree, F., Vosloo, W., Fick, W. & Huismans, H. (2011). The use of soluble African horse sickness viral protein 7 as an antigen delivery and presentation system. *Virus Res* **156**, 35-48.

Shelly, S., Lukinova, N., Bambina, S., Berman, A. & Cherry, S. (2009). Autophagy Is an Essential Component of Drosophila Immunity against Vesicular Stomatitis Virus. *Immunity* **30**, 588-598.

Stassen, L., Huismans, H. & Theron, J. (2012). African horse sickness virus induces apoptosis in cultured mammalian cells. *Virus Res* **163**, 385-389.

Stoltz, M. A., van der Merwe, C. F., Coetzee, J. & Huismans, H. (1996). Subcellular localization of the nonstructural protein NS3 of African horsesickness virus. *Onderstepoort J Vet Res* **63**, 57-61.

Studer, D., Graber, W., Al-Amoudi, A. & Eggli, P. (2001). A new approach for cryofixation by high-pressure freezing. *J Microsc* **203**, 285-294.

Uitenweerde, J. M., Theron, J., Stoltz, M. A. & Huismans, H. (1995). The Multimeric Nonstructural NS2 Proteins of Bluetongue Virus, African Horsesickness Virus, and Epizootic Hemorrhagic Disease Virus Differ in Their Single-Stranded RNA-Binding Ability. *Virology* **209**, 624-632.

Van der Merwe, C. F. & Coetzee, J. (1992). Quetol 651 for general use: a revised formulation. *Electron microscopy society of southern Africa* **22**, 31-32.

Venter, E., Van Der Merwe, C. F. & Van Staden, V. (2012). Utilization of cellulose microcapillary tubes as a model system for culturing and viral infection of mammalian cells. *Microsc Res Tech* **75**, 1452-1459.

Wechsler, S. J. & McHolland, L. E. (1988). Susceptibilities of 14 cell lines to bluetongue virus infection. *J Clin Microbiol* **26**, 2324-2327.

Wei, T., Hibino, H. & Omura, T. (2008). Rice dwarf virus is engulfed into and released via vesicular compartments in cultured insect vector cells. *J Gen Virol* **89**, 2915-2920.

Wirblich, C., Bhattacharya, B. & Roy, P. (2006). Nonstructural protein 3 of bluetongue virus assists virus release by recruiting ESCRT-I protein Tsg101. *J Virol* **80**, 460-473.

Yang, W. & McCrae, M. A. (2012). The rotavirus enterotoxin (NSP4) promotes re-modeling of the intracellular microtubule network. *Virus Res* **163**, 269-274.

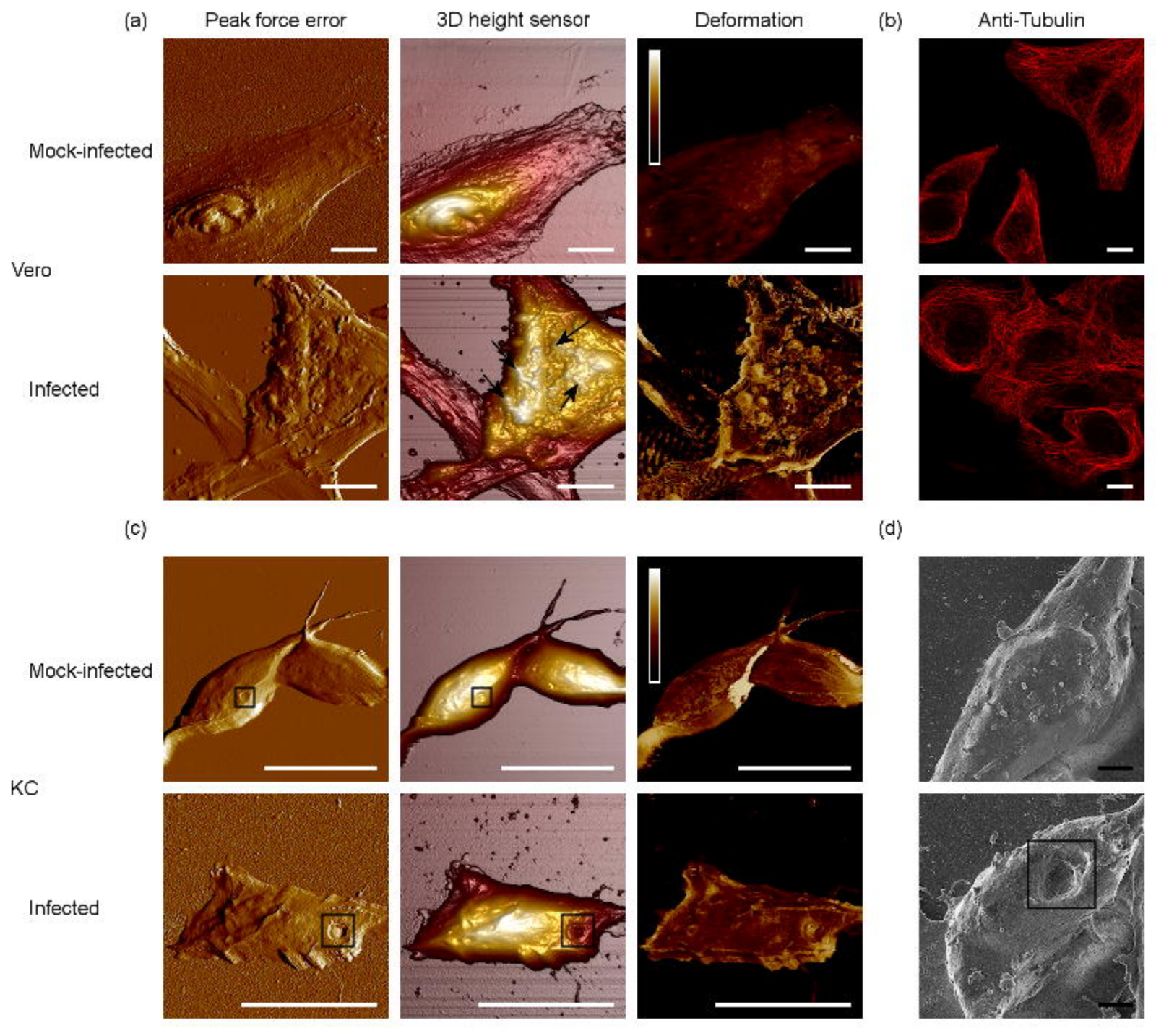
(a)
Peak force error
3D height sensor
Deformation
(b)
Anti-Tubulin
Mock-infected
Vero
Infected
(c)
(d)
Mock-infected
KC
Infected

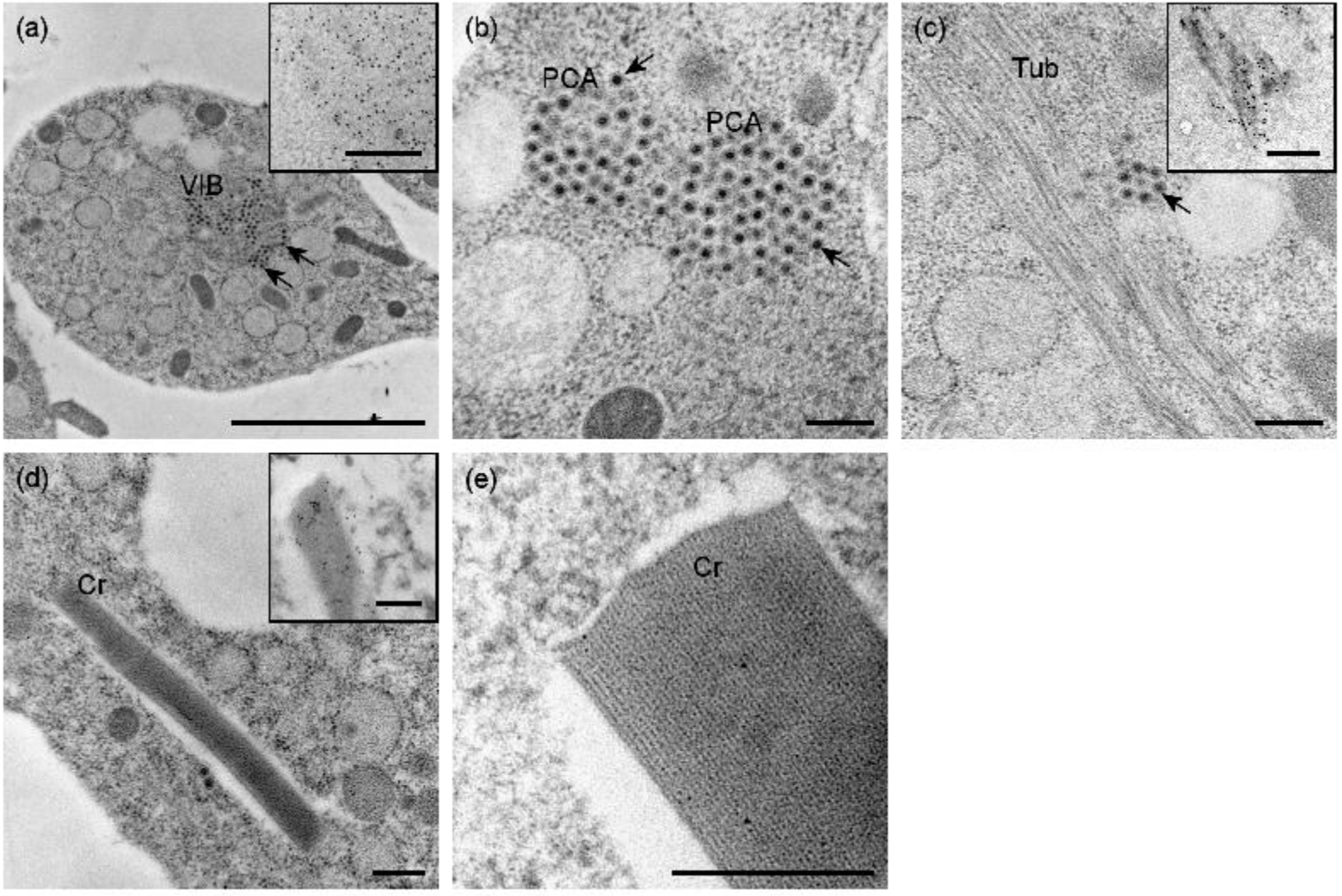
(a)
VIB
(b)
PCA
PCA
(c)
Tub
(d)
Cr
(e)
Cr

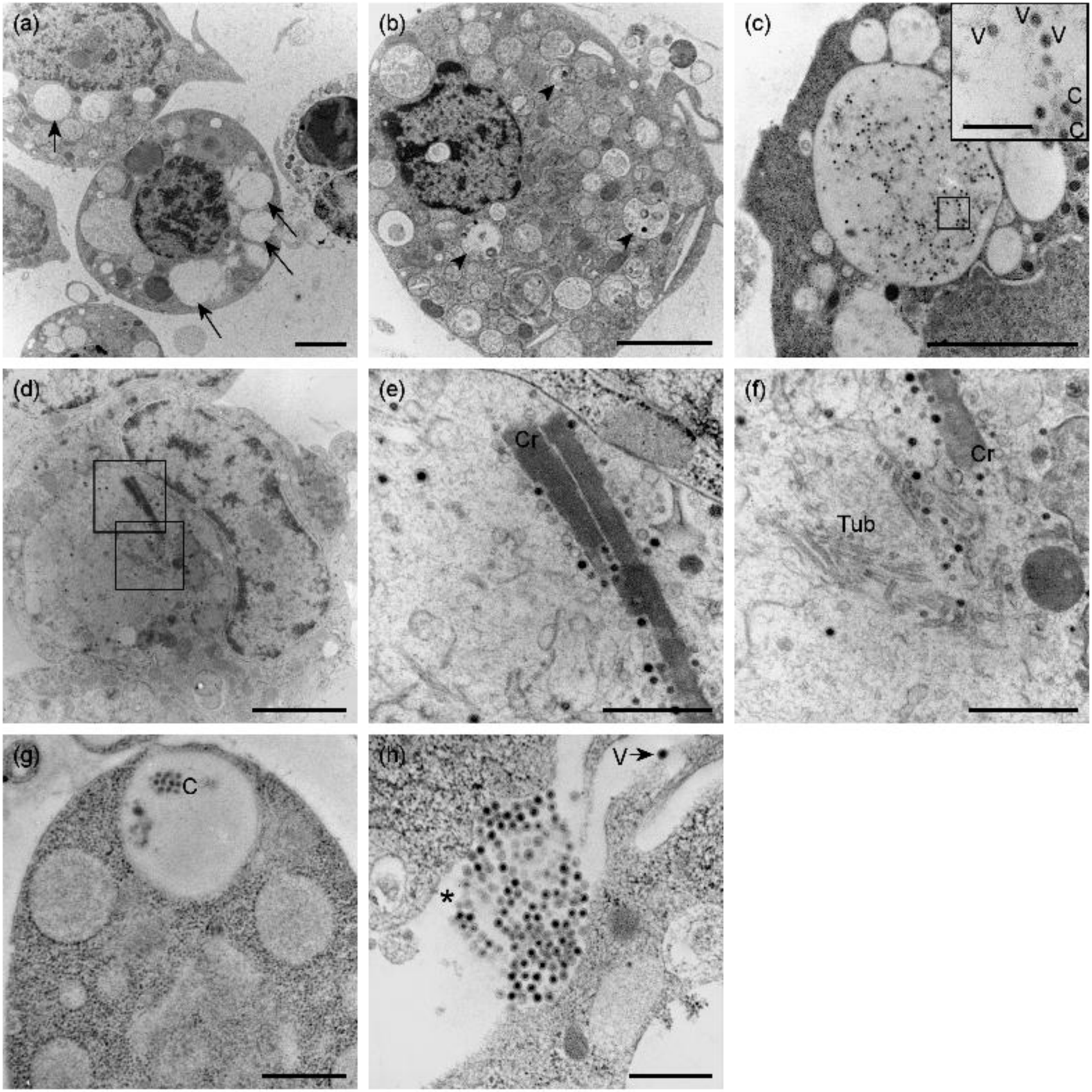
(a)
(b)
(c)
V
V
V
C
C
(d)
(e)
Cr
(f)
Cr
Tub
(g)
C
(h)
V
*

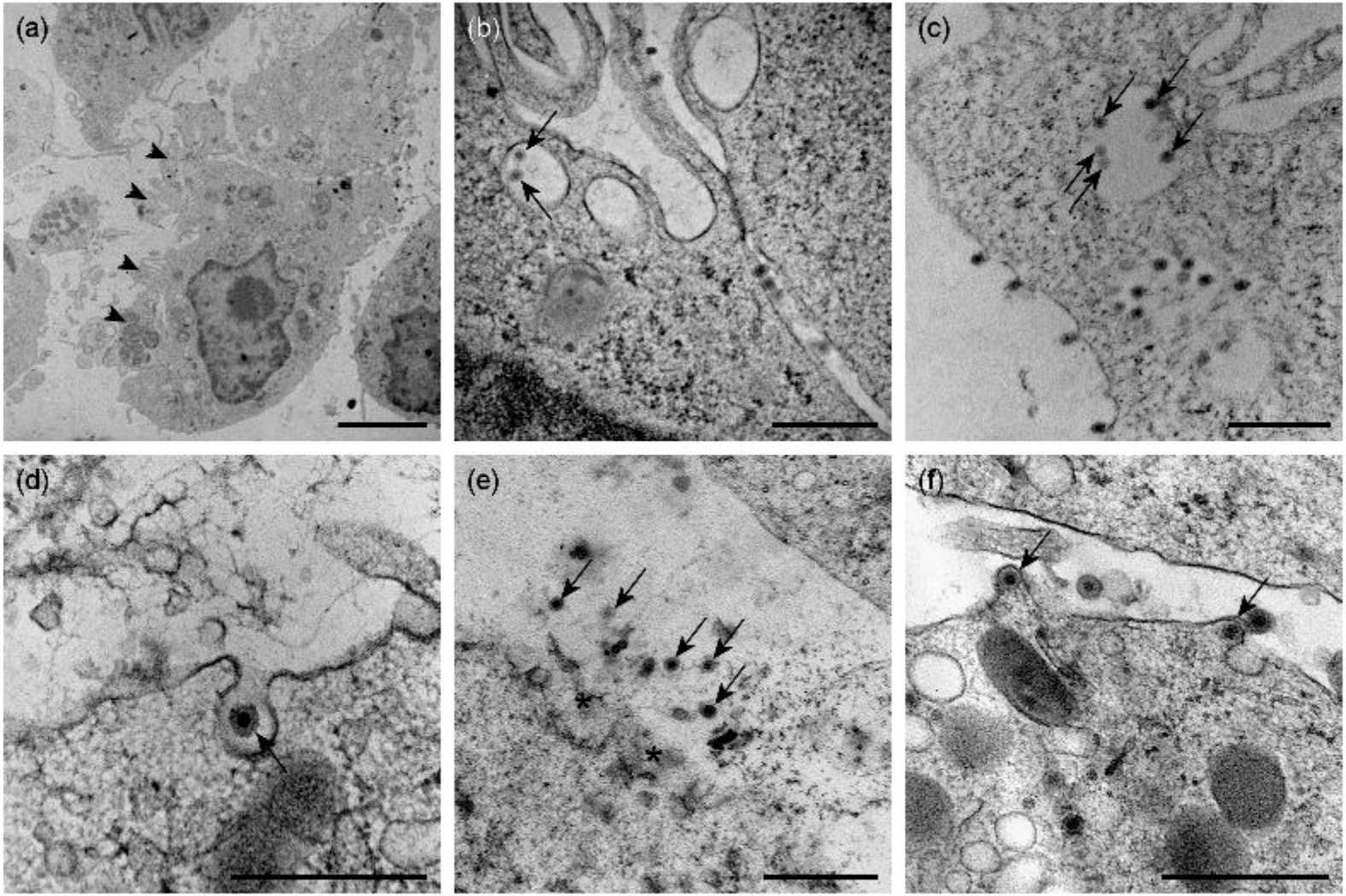
(a)
(b)
(c)
(d)
(e)
(f)